Ring compaction as a mechanism of densification in amorphous silica

Philip S. Salmon [1,*], Anita Zeidler [1], Motoki Shiga [2,3], Yohei Onodera [4,5] and Shinji Kohara [5]

[1]*Department of Physics, University of Bath, Bath BA2 7AY, United Kingdom*
[2]*Unprecedented-scale Data Analytics Center, Tohoku University, 468-1 Aramaki-Aza-Aoba, Aoba-ku, Sendai 980-8578, Japan*
[3]*Center for Advanced Intelligence Project, RIKEN, 1-4-1 Nihonbashi, Chuo-ku, Tokyo 103-0027, Japan*
[4]*Institute for Integrated Radiation and Nuclear Science, Kyoto University, 2-1010 Asashiro-nishi,*
Kumatori-cho, Sennan-gun, Osaka 590-0494, Japan
[5]*Research Center for Advanced Measurement and Characterization, National Institute for Materials Science (NIMS), Ibaraki 305-0047, Japan*

The structure of permanently densified silica glass is investigated by neutron and x-ray diffraction, and by the production of atomistic models that reproduce the diffraction results. The focus is on the nature of the ordering on an intermediate length scale that originates from the formation of n-rings, where n is the number of Si or O atoms within a ring. The densification process has a large effect on this ordering, as identified by pronounced changes to the first sharp diffraction peak (FSDP) in the measured structure factors. A clear and systematic dependence of the distribution of ring sizes on the position and shape of the FSDP could not be found, i.e., the ring statistics are not directly encoded into the form of this peak. Instead, a significant contribution to the glass densification originates from compaction of the n-rings, a metric that is quantified by the radius of gyration and lifetime of the rings. We thereby uncover and quantify a key densification mechanism in amorphous materials.

I. INTRODUCTION

Amorphous networks provide the foundation for a broad swath of functional glasses in energy and information technology [1] and provide the basis for the silicate magmas encountered in geoscience [2]. Fundamental to understanding the structure-function relationships is knowledge of the network structures and how they adapt as the state conditions are changed. Here, densification by pressure at room or elevated temperature is an important process that is encountered in the likes of sharp contact loading, when glass is indented or scratched, and when magma is confined below the Earth's surface. It is therefore important to understand the mechanisms of pressure-induced deformation as a first step in predicting the material's response.

The structural organization of the atoms in amorphous network-forming materials such as silica occurs on three different length scales, which manifest themselves as separate peaks in the structure factor $S(k)$ measured in a diffraction experiment, where k is the magnitude of the scattering vector. Three peaks appear at $k_1 r_0 = 2$–3, $k_2 r_0 = 4.6$–4.9, and $k_3 r_0 = 7.8$–8.9, where r_0 is the nearest-neighbor distance, and correspond to ordering on real-space length scales that are associated with the nearest-neighbor distance ($i = 3$), the size of the local structural motifs ($i = 2$), and the size of

the ring structures that are formed by the agglomeration of these motifs on an intermediate length scale ($i = 1$) [3,4]. In general, there will be a distribution of ring sizes that depends on the chemical composition of the glass and its temperature and/or pressure history. It is therefore appealing to search for a measure of this distribution in the shape of the $i = 1$ peak in $S(k)$, which is often known as the first sharp diffraction peak (FSDP) [5–7].

The ring structures can be identified by a closed path search along the chemical bonds in a material [8–13]. The ring size is defined by the number of nodes n that it contains. In silica glass, these nodes are usually identified with the Si atoms at the center of corner-sharing tetrahedral $SiO_{4/2}$ units. In general, each ring will have a characteristic length scale ℓ_n that increases with the number of nodes. If there is a large proportion of such rings, they are anticipated to modulate the number density of the material on this length scale. Hence there should be a contribution to the FSDP from a peak at position $2\pi/\ell_n$. This idea forms the basis of the recent work of Shi *et al.* [14] on silicate glasses, where the proportion of rings with $n \leqslant 4$, $n = 5$, and $n \geqslant 6$ was estimated from the shape of the FSDP measured in neutron diffraction experiments by using a fitting procedure in which the contribution from n-rings is assumed to scale with the proportion of those rings present in the network structure. The results were found to correlate with the Guttman ring statistics obtained from molecular dynamics (MD) simulations.

The findings of Shi *et al.* [14] are, however, far from obvious.

First, they require that the structural information represented by n-body ring correlations is "collapsed" into $S(k)$, which is a two-body correlation function. It is, however, notoriously difficult to gain accurate information on three-body

---

(bond-angle distributions), four-body (dihedral angle distributions), and higher body correlations simply from knowledge about the ensemble averaged distances between pairs of atoms. Indeed, it is possible to generate substantially different structural models that have an identical $S(k)$ function [15], i.e., there is no reason to presuppose a one-to-one correspondence between the shape of the FSDP and the ring statistics. This scenario is supported by previous work on fused silica [16] and is illustrated by the recent work of Shi *et al.* [17] in which MD simulations, designed to reproduce measured neutron diffraction patterns, deliver an identical FSDP to experiment, but also deliver substantially different ring-size distributions to those obtained from an analysis of the measured FSDP using the fitting procedure described in Ref. [14]. Additionally, the periodic real-space density fluctuations that give rise to the FSDP will not, in general, emanate from a set of connected rings having the same length scale as supposed in Ref. [14]. Instead, rings of different sizes will be interconnected, so the periodic density fluctuations that originate the FSDP must depend on the nature of this connectivity.

Second, the shape of the FSDP will depend on whether neutron or x-ray diffraction is used to measure the structure of the glass (Sec. III). Here, it is not obvious why the ring statistics should be encoded solely in the neutron diffraction results and why x-ray diffraction results should be precluded from the analysis [14]. Indeed, even in the case of neutron diffraction, the amplitude and shape of the measured FSDP can be altered substantially by changing the isotopic enrichment of the elements that are present—a variation that will have no effect on the chemical bonding or network structure [15]. This feature provides the cornerstone for the method of neutron diffraction with isotope substitution, which can be used to unravel the structural complexity of network-forming glasses such as SiO_2 and GeO_2 [18,19].

We have therefore been motivated to investigate the dependence of the FSDP on the ring statistics for vitreous silica, a prototypical network-forming glass that provides the foundation for the silicate class of amorphous materials. Specifically, we consider the recent diffraction work by Onodera *et al.* [20] in which the hot versus cold compression routes were used to systematically manipulate the network structure and thereby deliver FSDPs with significantly different positions and shapes. If the working hypothesis of Shi *et al.* [14] holds true, an increase in the proportion of smaller n-rings with density must facilitate an increase in the position k_1 of the FSDP.

This paper is organized as follows. The x-ray and neutron diffraction results of Onodera *et al.* [20] are summarized in Sec. II and are supplemented by new results for the pristine glass. New atomistic models for the glass structures are then developed in Sec. III. The ring statistics are presented in Sec. IV. The glass densification mechanisms are discussed in Sec. V where measures of the ring compaction are introduced. Conclusions are drawn in Sec. VI.

II. X-RAY AND NEUTRON DIFFRACTION

Cold compressed glasses were compacted at room temperature (RT) and a pressure of either 7.7 GPa or 20 GPa before they were recovered to ambient conditions [20]. Hot

TABLE I. Density, compaction, and oxygen packing fraction for the silica glasses. The compaction is given by the reduced density ρ/ρ_0, where ρ_0 is the density of the pristine (RT/0 GPa) glass. The oxygen packing fraction η_O [21] is calculated for tetrahedral $SiO_{4/2}$ motifs with an Si-O bond length of 1.614 Å. The measurement error on the density is ± 0.01 g cm^{-3}.

Glass	Density ρ (g cm^{-3})	ρ/ρ_0	η_O
RT/0 GPa	2.21	1.000	0.425
RT/7.7 GPa	2.24	1.014	0.430
400 °C/7.7 GPa	2.54	1.149	0.488
600 °C/7.7 GPa	2.66	1.204	0.511
800 °C/7.7 GPa	2.68	1.213	0.515
1000 °C/7.7 GPa	2.69	1.217	0.517
1200 °C/7.7 GPa	2.72	1.231	0.523
RT/20 GPa	2.71	1.226	0.521

compressed glasses were compacted at a pressure of 7.7 GPa and a temperature in the range from RT to 1200 °C before they were recovered to ambient conditions. The glasses are designated by the processing procedure, e.g., RT/20 GPa refers to the glass compacted at room temperature and a pressure of 20 GPa. The sample preparation conditions lead to glass densities that are up to 23% greater than the density of the pristine material, which will be designated by RT/0 GPa
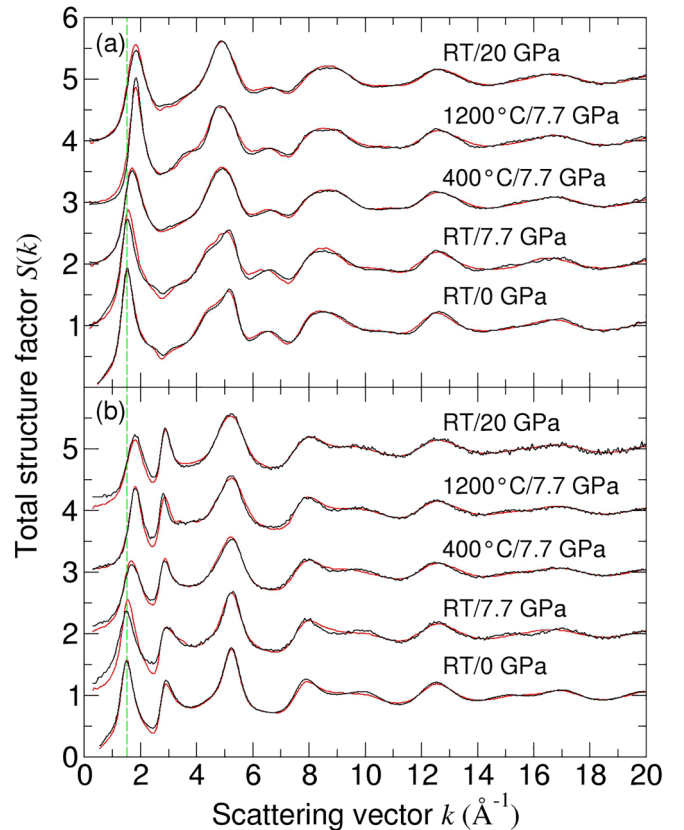
FIG. 1. Total structure factors $S(k)$ for the silica polyamorphs investigated using both (a) x-ray diffraction and (b) neutron diffraction (black solid curves). The red solid curves show the structure factors obtained from the MD-RMC models. The green vertical broken line marks the position of the FSDP for the RT/0 GPa glass.
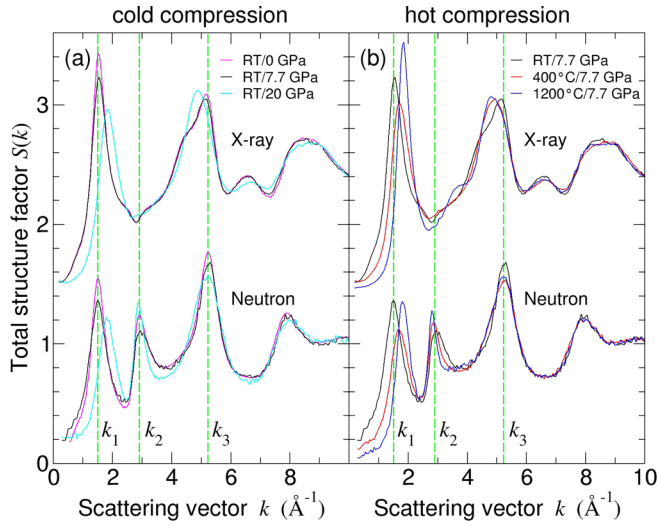
FIG. 2. X-ray and neutron $S(k)$ functions measured for the (a) cold and (b) hot compressed SiO_2 glasses in the region of the first three peaks with the positions k_1, k_2, and k_3. The green vertical broken lines mark the position of these peaks in the neutron $S(k)$ function for the RT/0 GPa glass.

(Table I). The structure factors for the pristine glass were measured using the high-energy x-ray diffraction beamline BL04B2 at SPring-8 [22] and the neutron diffractometer GEM at ISIS [23]. The structure factors for the densified glasses are taken from Ref. [20].

Figure 1 shows the measured x-ray and neutron total structure factors for the pristine and several of the densified SiO_2 glasses, where [15]

$$S(k) = 1 + \frac{1}{|\langle w(k) \rangle|^2} \sum_\alpha \sum_\beta c_\alpha c_\beta w_\alpha^*(k) w_\beta(k) [S_{\alpha\beta}(k) - 1], \quad (1)$$

c_α is the atomic fraction of chemical species α (Si or O), $w_\alpha(k)$ is the x-ray atomic form factor with dispersion terms or the neutron coherent scattering length of chemical species α, $S_{\alpha\beta}(k)$ is a partial structure factor for the chemical species α and β, and $|\langle w(k) \rangle|^2 = \sum_\alpha \sum_\beta c_\alpha c_\beta w_\alpha^*(k) w_\beta(k)$.

Figure 2 zooms into the region of the first three peaks in $S(k)$. The position of the FSDP increases monotonically with the density as shown in Fig. 3(a). On cold compression, the height of the FSDP decreases with increasing pressure as the peak broadens. In contrast, on hot compression the height of the FSDP first decreases and then increases with the processing temperature, i.e., there is a broadening followed by a sharpening of this feature [Fig. 3(b)].

The corresponding real-space total-correlation functions are shown in Fig. 4. They were obtained from the Fourier transform

$$T(r) = 4\pi n_0 r + \frac{2}{\pi} \int_0^\infty dk [S(k) - 1] M(k) k \sin(kr), \quad (2)$$

where r is a distance in real space, n_0 is the atomic number density, and $M(k)$ is the Lorch [24] modification function given by $M(k) = \sin(\pi k / k_{max}) / (\pi k / k_{max})$ for $k \leqslant k_{max}$ and $M(k) = 0$ for $k > k_{max}$, where k_{max} is the maximum value of
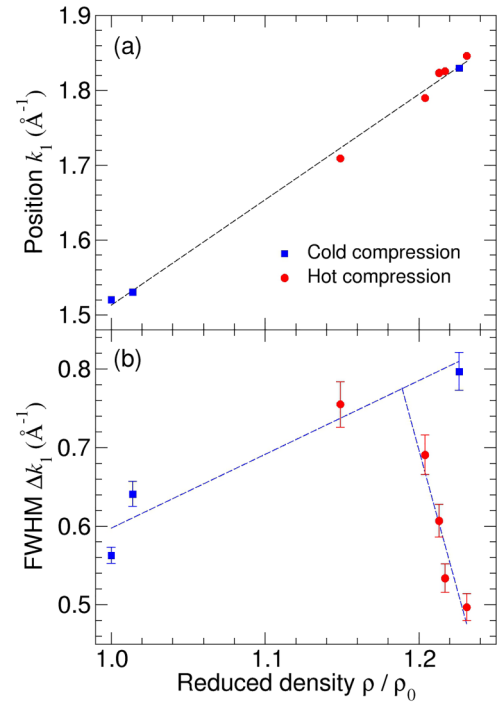
FIG. 3. Reduced density dependence of (a) the position k_1 and (b) the full width at half maximum Δk_1 of the FSDP for the different polyamorphs of silica glass extracted from the x-ray $S(k)$ functions. In (a), the error bars are smaller than the symbol size and the fitted line $k_1(\text{Å}^{-1}) = 1.41(4)\rho/\rho_0 + 0.10(5)$ shows an approximately linear relationship between the peak position and density. In (b), the lines are drawn as guides to the eye.

k. The first peak in the measured $T(r)$ functions originates from Si-O correlations and gives an Si–O coordination number of four within the experimental error, which indicates a network built from tetrahedral $SiO_{4/2}$ units. The Si-O bond length remains invariant within the experimental error, with a mean value of 1.614(3) Å, and there is little change to
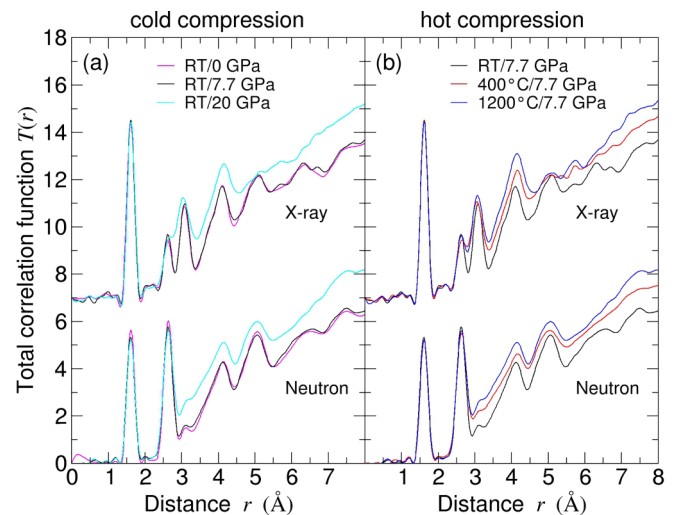
FIG. 4. X-ray and neutron $T(r)$ functions measured for the (a) cold and (b) hot compressed SiO_2 glasses ($k_{max} = 23.45$ Å^{-1}).
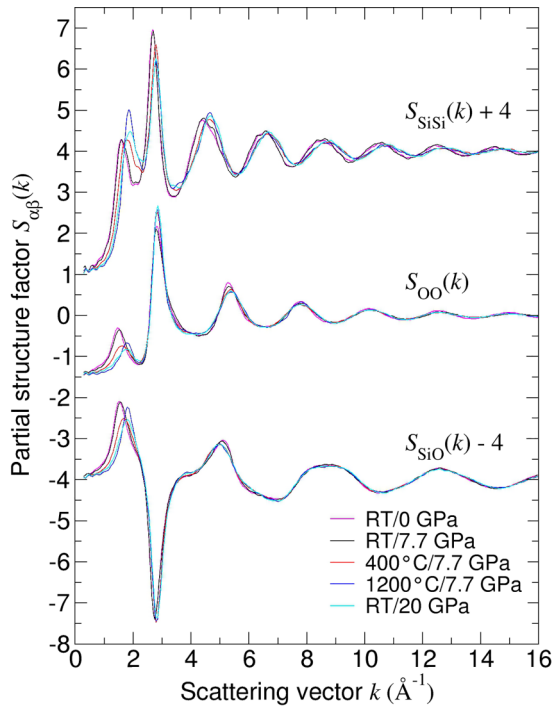
FIG. 5. Partial structure factors $S_{\alpha\beta}(k)$ obtained from the MD-RMC models for the different polyamorphs of silica glass.

FIG. 6. Contributions of the weighted partial structure factors $S_{\alpha\beta}(k)$ [see Eq. (1)] towards the (a) and (b) x-ray versus (c) and (d) neutron total structure factors $S(k)$ for identical MD-RMC structural models of either the pristine (left column) or RT/20 GPa (right column) glass. The weighting factors were calculated using neutron scattering lengths of $b_{Si} = 4.1491(10)$ fm and $b_O = 5.803(4)$ fm [25] or neutral atom x-ray form factors taken from Ref. [26]. To emphasize the different FSDP shapes measured by x-ray and neutron diffraction for a given glass, the neutron $S(k)$ functions are shown by the broken magenta curves in (a) and (b), and the x-ray $S(k)$ functions are shown by the broken magenta curves in (c) and (d).

the shape of the first peak in $T(r)$. Glass densification does not therefore originate from a large change to the tetrahedral SiO$_{4/2}$ units, e.g., it does not originate from the compression of those units. The packing of the tetrahedral units does, however, increase with the glass density, as manifested by an increase in the oxygen packing fraction η_O [21] (Table I).

III. ATOMISTIC MODELS

The atomistic structure of the pristine and densified materials was also probed by performing MD simulations on systems of 9000 atoms and by employing the diffraction data to refine the models thus obtained via the reverse Monte Carlo (RMC) method. The models were developed using the protocols described in Ref. [20], except that the large-scale atomic/molecular massively parallel simulator (LAMMPS) code [27] was used for the MD simulations and the system size was three times larger in order to improve the statistical significance of the modeled parameters. In the MD method, a model for the pristine glass was first created. It was then either cold or hot compressed, following a procedure designed to mimic the experimental work. Bond-switching (or other) restrictions were not applied, i.e., a given system was allowed to evolve according to the state conditions and was free to change the connectivity of its silicon-centered structural motifs. The simulation timescale under cold compression (~100 ps) was sufficiently long to enable a substantial reorganization of the ring statistics, provided the state conditions allow for it [28]. In the RMC refinements, the Si-O coordination number distributions and intratetrahedral O-Si-O bond angle distributions from the MD simulations were used as constraints. These restrictions ensured the creation of networks of predominantly corner-sharing tetrahedral SiO$_{4/2}$

units, consistent with the experimental findings. The models give a good account of the diffraction data as shown in Fig. 1.

The results show that all the partial structure factors contribute towards the FSDP (Fig. 5), with weighting factors that depend on whether the structural probe is x-ray or neutron diffraction (Fig. 6). This weighting accounts for the difference in amplitude and shape of the FSDPs measured by x-ray versus neutron diffraction. It also accounts for the presence of a principal peak at k_2 in the neutron $S(k)$ functions but an absence of this feature in the corresponding x-ray $S(k)$ functions. We note that there will also be a contribution to the different peak shapes from the k-space resolution function of the x-ray or neutron diffractometer [29]. In the case of neutron diffraction, the shape of the FSDP in $S(k)$ can also be changed by altering the isotopic enrichment of Si and/or O and hence the relative weighting of the contributing partial structure factors [19,30].

Figure 7 shows the bond angle distributions $B(\theta)$ obtained from the MD-RMC models, where this distribution is either (a) un-normalized or (b) normalized by a factor of $\sin(\theta)$. Each distribution $B(\theta)$ is proportional to the number of bonds found between angles of θ and $\theta + \Delta\theta$, which will depend on the solid angle subtended at that value of θ during the sampling procedure. The latter is proportional to $\sin(\theta)$ and it is therefore appropriate to remove its effect by plotting the distribution as $B(\theta)/\sin(\theta)$ so that peaks are not distorted, e.g., a finite bond angle distribution at $\theta \simeq 180°$ will not be artificially suppressed [31,32].

The MD-RMC models give intratetrahedral O–Si–O bond-angle distributions with a peak position around 109°, which is
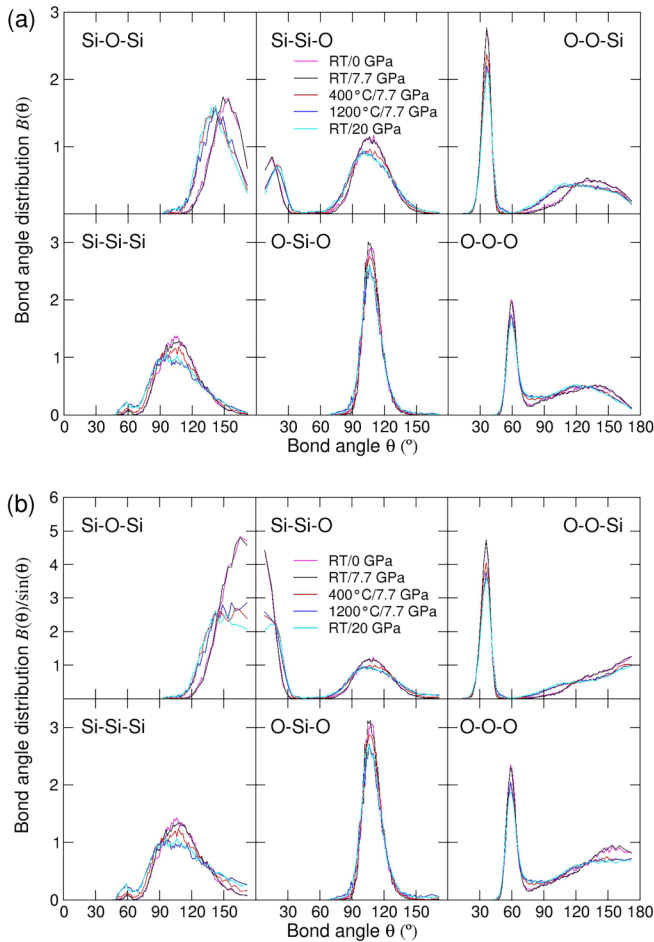
FIG. 7. Bond angle distributions (a) $B(\theta)$ and (b) $B(\theta)/\sin(\theta)$ obtained from the MD-RMC models for the different polyamorphs of silica glass. In (b), the normalization by $\sin(\theta)$ takes into account the solid-angle subtended when sampling the bond angles and avoids an artificial suppression of distributions that contain large bond angles (see Sec. III).

consistent with a network built from tetrahedral $SiO_{4/2}$ units. These units are not, however, uniform as indicated by the finite width of the intratetrahedral O–Si–O bond-angle distribution and by the finite width of the nearest-neighbor Si-O peak in $T(r)$ (Fig. 4). The intertetrahedral Si–O–Si bond-angle distribution indicates corner-sharing motifs. The maximum in $B(\theta)$ at $\theta \simeq 154(2)°$ for the pristine glass compares to a value in the range 148–153° reported in previous work [33,34]. The peak position decreases with increasing density, consistent with the findings from experiment [35] and with previous MD [36,37] and Monte Carlo [38] simulations of compacted silica glass. As discussed below, the $SiO_{4/2}$ units will connect to form n-rings, where the shape of a given ring will depend on the precise shape of the $SiO_{4/2}$ tetrahedral units from which it is formed and the value of the intertetrahedral Si–O–Si bond angle.

IV. RING STATISTICS

The ring statistics in the MD-RMC models were probed by using the R.I.N.G.S. code [12,13]. In this analysis, King
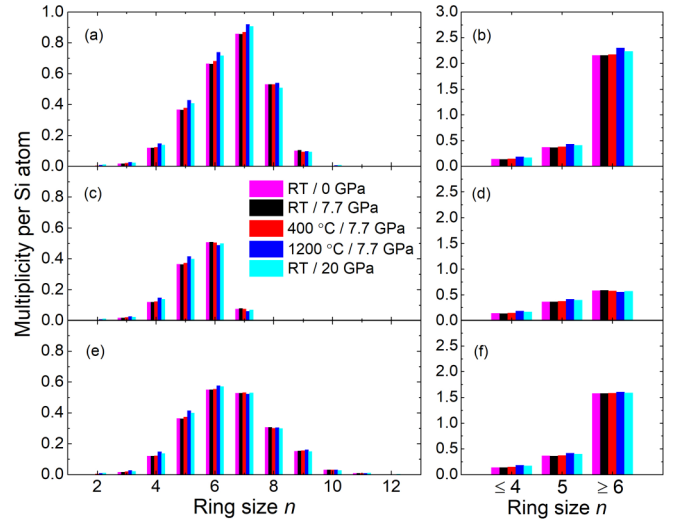
FIG. 8. Full (left-hand column) versus grouped (right-hand column) distributions of ring sizes for the different polyamorphs of silica glass. The distributions correspond to (a) and (b) King rings, (c) and (d) Guttman rings, or (e) and (f) primitive rings.

rings [8], Guttman rings [9], and primitive rings [10] were all calculated. For a given starting node, Guttman rings are found by following the Si-O bonds and tracing the shortest path back to the starting node from a specified nearest-neighbor, whereas King rings are found by following the Si-O bonds and tracing the shortest path between two specified nearest neighbors of the starting node. Primitive rings also represent
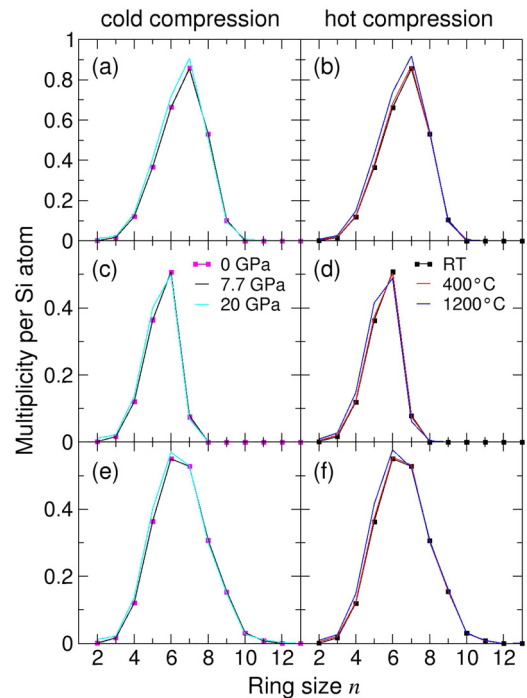
FIG. 9. Distributions of (a) and (b) King rings, (c) and (d) Guttman rings, or (e) and (f) primitive rings for the different polyamorphs of silica glass under cold compression at RT (left column) or hot compression at 7.7 GPa (right column).
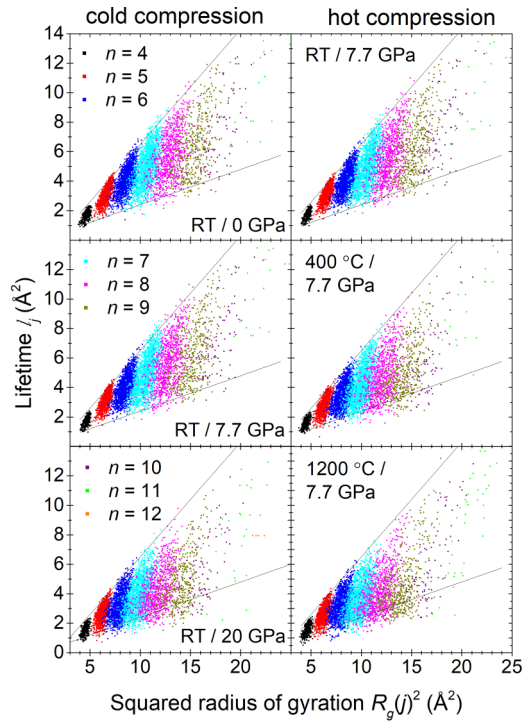
FIG. 10. Silicon-centric scatter plot of the squared radius of gyration $R_g(j)^2$ versus the lifetime l_j of the primitive n-rings found for the cold compressed (first column) versus hot compressed (second column) SiO_2 glasses. The sloped straight lines mark the approximate envelope of the data sets for the RT/0 GPa glass.

FIG. 11. Oxygen-centric scatter plot of the squared radius of gyration $R_g(j)^2$ versus the lifetime l_j of the primitive n-rings found for the cold compressed (first column) versus hot compressed (second column) SiO_2 glasses. The sloped straight lines mark the approximate envelope of the data sets for the RT/0 GPa glass.

closed paths, but they cannot be decomposed into smaller rings [11].

The results show that it is hard to associate the dramatic changes that occur to the position and shape of the FSDP under hot or cold compression (Fig. 2) with systematic trends in the ring statistics that are independent of the ring definition (Figs. 8 and 9).

On hot compression at 7.7 GPa, for example, the proportions of $n = 4$ and $n = 5$ rings both increase with the temperature (or density) irrespective of the ring definition, but the proportion of $n = 6$ rings either increases (King and primitive) or decreases (Guttman) and the proportion of $n = 7$ rings either increases (King), decreases (Guttman), or first increases and then decreases (primitive) (Fig. 8). If the rings are placed into groups with $n \leqslant 4$, $n = 5$, or $n \geqslant 6$ (as in Ref. [14]), the proportion of $n \geqslant 6$ rings either increases (King and primitive) or decreases (Guttman) with increasing density. On cold compression at RT, a similar variation in behavior can be observed. For example, the proportion of $n = 7$ rings either decreases then increases (King), increases then decreases (Guttman), or remains more-or-less invariant (primitive) as the pressure is increased (Fig. 8). The proportion of $n \geqslant 6$ rings either increases then decreases (Guttman) or remains constant before increasing (King and primitive) with increasing density.

For the most compacted similar-density 1200 °C/7.7 GPa and RT/20 GPa glasses (Table I), where the FSDP positions are similar but there is contrast between the peak widths (Fig. 3), the relative proportion of $n \geqslant 6$ rings is larger or
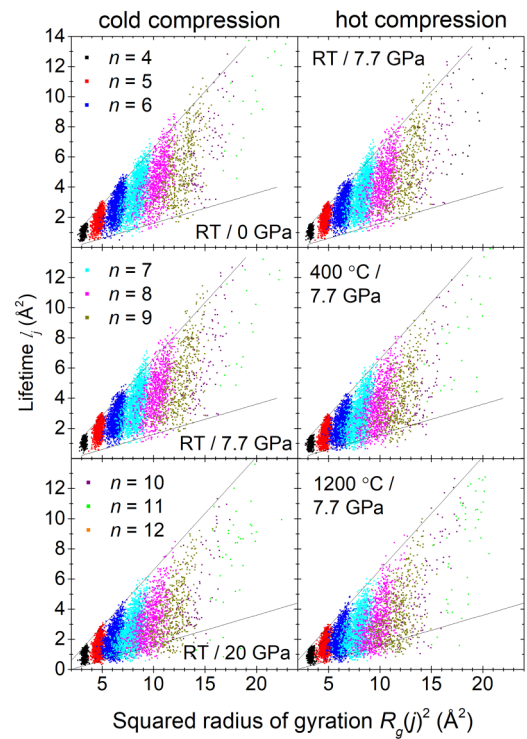
smaller, depending on the choice of ring type (Fig. 8). The large density of these glasses is, however, associated with a shift in the ring-size distributions towards smaller ring sizes (Fig. 9).

The observed increase in the number of $n = 3$ and $n = 4$ rings with density (Fig. 8) is consistent with a measured increase of intensity associated with the D_1 and D_2 "defect" lines in the Raman spectra for silica at 495 and 606 cm^{-1}, respectively [35,39], which originate from the $n = 4$ and $n = 3$ rings, respectively [40,41]. According to Rahmani *et al.* [42], however, the peak areas are not simply proportional to the concentration of these small rings.

In comparison, a variety of behavior is indicated from previous MD and Monte Carlo models of silica glass, which reflects the use of different atomic interaction models and/or sample preparation procedures. Investigations show, for example, (i) a monotonic shift towards smaller ring sizes at pressures up to 57.5 GPa on cold compression at 27 °C for models that reproduce the measured equation of state [28], (ii) no discernible change to the ring-size distribution from 15 to 20 GPa at 227 °C [36], (iii) a shift of the distribution towards larger ring sizes over the 15 to 20 GPa pressure range as the temperature is raised from 727 to 1727 °C [37], (iv) a shift towards larger ring sizes on cold compression at $\geqslant 5$ GPa and 27 °C [38], (v) a shift towards larger ring sizes at pressures $\geqslant 16$ GPa on "cold" compression at 727 °C or on hot compression at 8 GPa and a higher temperature [43], or (vi) a shift towards larger ring sizes on quenching from the
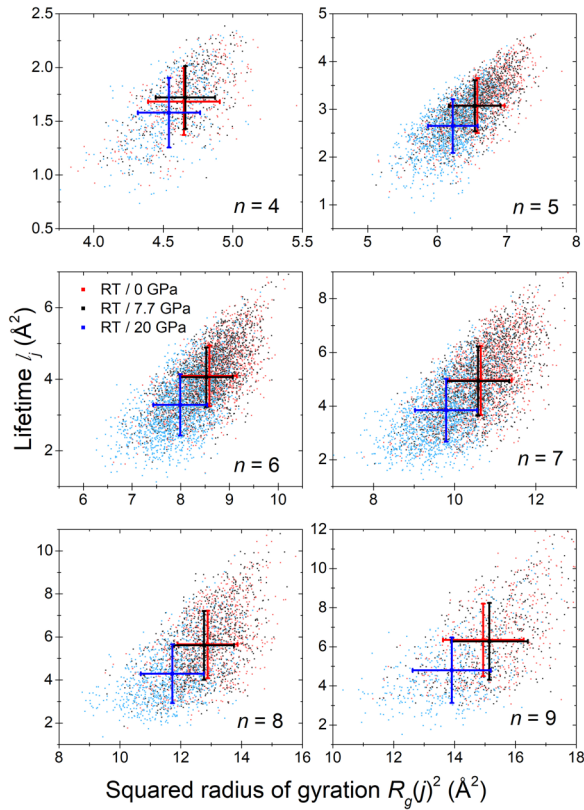
FIG. 12. Silicon-centric scatter plot of the squared radius of gyration $R_g(j)^2$ versus the lifetime l_j of the primitive n-rings found for the cold compressed SiO_2 glasses with $n = 4$–9. For each glass, the small squares show the individual data points and the large square marks the mean values of $\langle R_g(j)^2 \rangle$ and $\langle l_j \rangle$. The horizontal and vertical bars show the standard deviation of each distribution about the mean.

FIG. 13. Oxygen-centric scatter plot of the squared radius of gyration $R_g(j)^2$ versus the lifetime l_j of the primitive n-rings found for the cold compressed SiO_2 glasses with $n = 4$–9. For each glass, the small squares show the individual data points and the large square marks the mean values of $\langle R_g(j)^2 \rangle$ and $\langle l_j \rangle$. The horizontal and vertical bars show the standard deviation of each distribution about the mean.

melt at 3727 °C for pressures up to 18 GPa followed by a shift towards smaller ring sizes on quenching from the melt at larger pressures [28].

Overall, the results do not support the notion that the ring statistics can be reliably obtained from the position and shape of the FSDP. For instance, the RT/7.7 GPa and 400 °C/7.7 GPa materials have contrasting FSDPs (Fig. 2) but essentially the same ring statistics (Fig. 9). It is not clear that the FSDP in the diffraction patterns is particularly sensitive to the presence of Guttman rings as reported elsewhere [14,17,44].

V. MECHANISMS OF GLASS DENSIFICATION

The present analysis shows that the ring-size distribution does not change substantially for the different network structures, although there is a shift towards smaller ring sizes for the highest density materials (Fig. 9). An explanation lies with the pressure range covered in the compression procedure, in that few fivefold or sixfold Si sites are created at pressures up to 20 GPa [28,45–47]. There will also be relaxation of the network structure when the glass is recovered from high-pressure to ambient conditions and a corner-sharing network of tetrahedral $SiO_{4/2}$ motifs is regained. Nevertheless, the
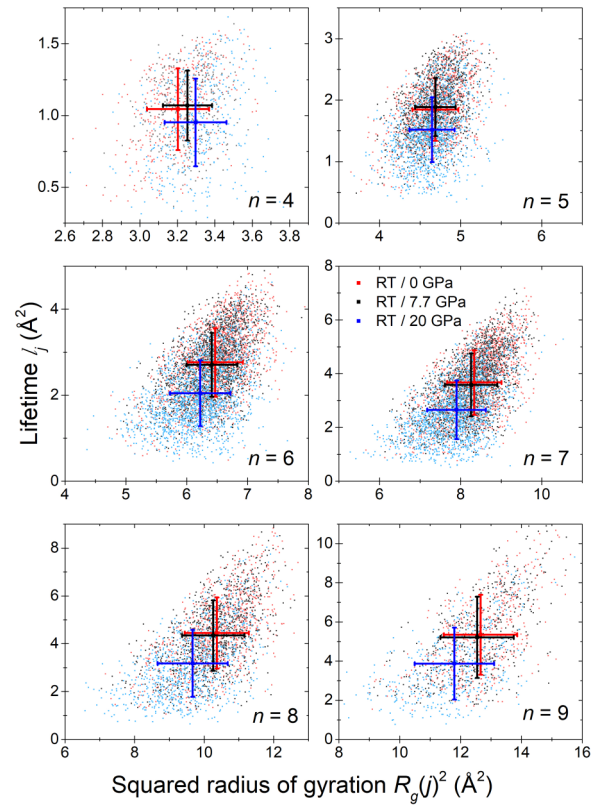
network is permanently densified, so the shape of the rings must adjust in response to the reduced volume.

To quantify the degree of ring compaction, the radius of gyration $R_g(j)$ was calculated for each of the primitive rings j, where

$$R_g(j)^2 = \frac{1}{N} \sum_{k=1}^{N} [\mathbf{r}_k(j) - \langle \mathbf{r}_k(j) \rangle]^2, \qquad (3)$$

N is the number of designated atoms (Si or O) within ring j, $\mathbf{r}_k(j)$ is the position of the kth atom within ring j, and $\langle \mathbf{r}_k(j) \rangle$ is the mean position of these atoms. A more compact ring will have a smaller radius of gyration as compared to a less compact ring with the same number of nodes. The persistent homology technique [48] was also applied to each of the primitive rings. Here, a sphere is centered on the co-ordinates of each of the selected atoms (Si or O) forming a given ring j. The radius of the sphere is then uniformly increased from zero. The radius $r(b_j)$ at which all the spheres touch defines the birth coordinate $b_j = r(b_j)^2$ of that ring and is commensurate with the nearest-neighbor Si-Si or O-O distance. The radius $r(d_j)$ at which the hole in the ring is first covered by the overlapping spheres defines the death coordinate $d_j = r(d_j)^2$ of that ring and is commensurate with its overall size. The lifetime $l_j = d_j - b_j$ will depend on the
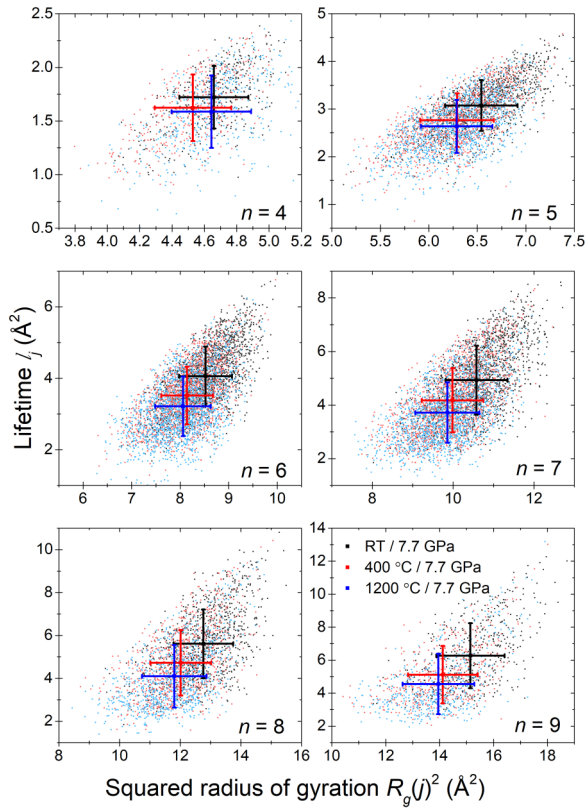
FIG. 14. Silicon-centric scatter plot of the squared radius of gyration $R_g(j)^2$ versus the lifetime l_j of the primitive n-rings found for the hot compressed SiO_2 glasses with $n = 4$–9. For each glass, the small squares show the individual data points and the large square marks the mean values of $\langle R_g(j)^2 \rangle$ and $\langle l_j \rangle$. The horizontal and vertical bars show the standard deviation of each distribution about the mean.

FIG. 15. Oxygen-centric scatter plot of the squared radius of gyration $R_g(j)^2$ versus the lifetime l_j of the primitive n-rings found for the hot compressed SiO_2 glasses with $n = 4$–9. For each glass, the small squares show the individual data points and the large square marks the mean values of $\langle R_g(j)^2 \rangle$ and $\langle l_j \rangle$. The horizontal and vertical bars show the standard deviation of each distribution about the mean.

ring size and its shape. For example, a regular planar 6-ring will have a longer lifetime than (i) a regular 6-ring with a shorter distance between the nodes or (ii) an elongated planar 6-ring having the same distance between the nodes [49].

Figures 10 and 11 show the Si- and O-centric scatter plots of $R_g(j)^2$ versus l_j for each of the glasses, respectively. The n-rings manifest themselves by distinct bands, showing that the ring lifetime increases with the radius of gyration. As compared to their Si-centric counterparts, the n-ring distributions in the O-centric scatter plots are shifted towards smaller $R_g(j)^2$ and l_j values. This difference between the Si- and O-centric viewpoints is anticipated. For example, in α-quartz under ambient conditions, the mean O-O and Si-Si distances within the 6-rings are 2.66 Å and 3.06 Å, respectively [50], i.e., the 6-ring formed by the Si sites is larger than that formed by the O sites. The radius of gyration is therefore smaller for the more compact ring formed by the O sites and the lifetime of this ring is correspondingly shorter. In either the Si- or O-centric representation, almost all the bands shift towards smaller $R_g(j)^2$ and l_j values with increasing density, which indicates ring compaction or buckling.

In order to elucidate the structural changes that occur, a scatter plot of $R_g(j)^2$ versus l_j was constructed for each glass for every ring size. The mean values $\langle R_g(j)^2 \rangle$ and $\langle l(j) \rangle$
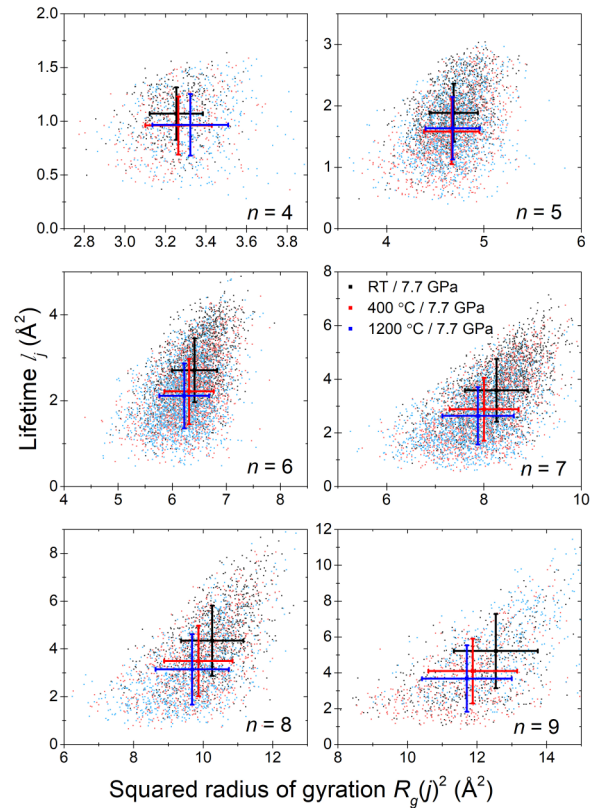
were calculated, along with the standard deviations about the mean.

Figures 12 and 13 show the Si- and O-centric scatter plots for the cold compressed glasses, respectively. Overall, there is little change to either $\langle R_g(j)^2 \rangle$ or $\langle l(j) \rangle$ as the pressure increases from ambient to 7.7 GPa. A reduction in the values of these parameters then occurs for almost all ring sizes as the pressure is increased further to 20 GPa. Hence compression has comparatively little effect on the shape of the rings until a threshold pressure >7.7 GPa is attained, consistent with the findings for the other structural parameters. A large change in ring compaction then occurs, which accounts for the shift in position of the FSDP towards a larger value of k_1 [Fig. 2(a)].

Figures 14 and 15 show the Si- and O-centric scatter plots for the hot compressed glasses, respectively. Here, the behavior of the n-rings is more complex, reflecting the ability of the ring structures to relax with increasing temperature. From the Si-centric viewpoint, the $\langle R_g(j)^2 \rangle$ and $\langle l(j) \rangle$ values for the $n = 4$ and 5 rings first decrease as the temperature is increased from ambient to 400 °C, and then either adjust or remain approximately the same as the temperature is increased further to 1200 °C. In comparison, the values of these parameters for the $n \geqslant 6$ rings decrease more steadily as the temperature is raised from ambient to 1200 °C. From the O-centric viewpoint, the

largest changes to the $\langle R_g(j)^2 \rangle$ and $\langle l(j) \rangle$ values for all the n-rings generally occur as the temperature is first increased from ambient to $400\,^\circ$C. In the case of the $n \geqslant 6$ rings, the $\langle R_g(j)^2 \rangle$ and $\langle l(j) \rangle$ values decrease with increasing temperature. The story for the $n = 4$ and 5 rings is more complex. The $\langle R_g(j)^2 \rangle$ value for the $n = 4$ rings enlarges as the temperature is increased from $400\,^\circ$C to $1200\,^\circ$C, reflecting a longer mean intraring O-O distance.

Overall, on hot compression the initial increase in temperature to $400\,^\circ$C affects the shape of all the rings. This compaction leads to a density for the $400\,^\circ$C/7.7 GPa glass that is greater than its cold compressed counterpart RT/7.7 GPa, resulting in an FSDP that is broader and shifted to a larger value of k_1 (Fig. 2). The subsequent increase in temperature to $1200\,^\circ$C and the concomitant sharpening of the FSDP [Fig. 2(b))] is related to further compaction of the larger $n \geqslant 6$ ring sizes.

We note that GeO_2 glass has been investigated under cold compression by *in situ* high-pressure neutron diffraction with isotope substitution, and the results were modeled using MD simulations with interaction potentials that include dipole-polarization effects [51]. For the pressure regime in which the glass network remains tetrahedral, corresponding to reduced densities $\rho/\rho_0 \lesssim 1.16$, the measured and simulated mean Ge-O-Ge bond angle decreases from $134.7(1.6)^\circ$ to $128.5(1.6)^\circ$ as the density is increased from its ambient value, but there is no change to the Ge-O bond length and little change to the ring statistics. The results therefore point to a pressure-induced reduction in the mean Ge-Ge distance within a ring, thereby supporting the notion that ring compaction is an important mechanism of densification in amorphous network-forming systems.

VI. CONCLUSIONS

In summary, the permanent densification of SiO_2 glass does not originate from a major change to the distribution of ring sizes. The ring statistics are not, therefore, directly encoded into the position and shape of the FSDP in $S(k)$, a finding that is supported by the difference in shape between the peaks measured by x-ray versus neutron diffraction for a given polyamorph and by the ability to change the shape of the FSDP in neutron diffraction for a given polyamorph by changing the isotopic enrichment of the elements.

Densification proceeds primarily via ring compaction, as assessed from the reduction in both the radius of gyration and lifetime of the rings with increasing density. On cold compression, there is little effect on the shape of the rings until a threshold pressure >7.7 GPa is attained. On hot compression, the sharpening of the FSDP at a temperature $>400\,^\circ$C is related to the compaction of the rings with $n \geqslant 6$.

The process of ring compaction or buckling under pressure should be common to silicates and other amorphous network-forming systems. It is, therefore, a likely mechanism for the mechanical deformation of these materials, for example, on sharp-contact loading [52–56] or in a geophysical environment where glass is often used as a proxy for uncovering the structural transformations [2,57,58]. The mechanism provides a pathway by which network modifiers can increase their coordination number.

The data sets created during this research are openly available from the University of Bath Research Data Archive [59].

[1] *Springer Handbook of Glass*, edited by J. D. Musgraves, J. Hu, and L. Calvez (Springer, Cham, 2019).

[2] *Magmas under Pressure*, edited by Y. Kono and C. Sanloup (Elsevier, Amsterdam, 2018).

[3] A. Zeidler and P. S. Salmon, Phys. Rev. B **93**, 214204 (2016).

[4] P. S. Salmon and A. Zeidler, J. Stat. Mech.: Theory Exp. (2019) 114006.

[5] S. R. Elliott, Nature (London) **354**, 445 (1991).

[6] P. S. Salmon, Proc. R. Soc. London A **445**, 351 (1994).

[7] P. H. Gaskell and D. J. Wallis, Phys. Rev. Lett. **76**, 66 (1996).

[8] S. V. King, Nature (London) **213**, 1112 (1967).

[9] L. Guttman, J. Non-Cryst. Solids **116**, 145 (1990).

[10] C. S. Marians and L. W. Hobbs, J. Non-Cryst. Solids **124**, 242 (1990).

[11] X. Yuan and A. N. Cormack, Comput. Mater. Sci. **24**, 343 (2002).

[12] S. Le Roux and P. Jund, Comput. Mater. Sci. **49**, 70 (2010).

[13] S. Le Roux and P. Jund, Comput. Mater. Sci. **50**, 1217 (2011).

[14] Y. Shi, J. Neuefeind, D. Ma, K. Page, L. A. Lamberson, N. J. Smith, A. Tandia, and A. P. Song, J. Non-Cryst. Solids **516**, 71 (2019).

[15] H. E. Fischer, A. C. Barnes, and P. S. Salmon, Rep. Prog. Phys. **69**, 233 (2006).

[16] L. P. Dávila, M.-J. Caturla, A. Kubota, B. Sadigh, T. Díaz de la Rubia, J. F. Shackelford, S. H. Risbud, and S. H. Garofalini, Phys. Rev. Lett. **91**, 205501 (2003).

[17] Y. Shi, B. Deng, O. Gulbiten, M. Bauchy, Q. Zhou, J. Neuefeind, S. R. Elliott, N. J. Smith, and D. C. Allan, Nat. Commun. **14**, 13 (2023).

[18] P. S. Salmon, A. C. Barnes, R. A. Martin, and G. J. Cuello, J. Phys.: Condens. Matter **19**, 415110 (2007).

[19] Q. Mei, C. J. Benmore, S. Sen, R. Sharma, and J. L. Yarger, Phys. Rev. B **78**, 144204 (2008).

[20] Y. Onodera, S. Kohara, P. S. Salmon, A. Hirata, N. Nishiyama, S. Kitani, A. Zeidler, M. Shiga, A. Masuno, H. Inoue, S. Tahara, A. Polidori, H. E. Fischer, T. Mori, S. Kojima, H. Kawaji,

A. I. Kolesnikov, M. B. Stone, M. G. Tucker, M. T. McDonnell *et al.*, NPG Asia Mater. **12**, 85 (2020).

[21] A. Zeidler, P. S. Salmon, and L. B. Skinner, Proc. Natl. Acad. Sci. U.S.A. **111**, 10045 (2014).

[22] K. Ohara, Y. Onodera, M. Murakami, and S. Kohara, J. Phys.: Condens. Matter **33**, 383001 (2021).

[23] A. C. Hannon, Nucl. Instrum. Methods Phys. Res., A **551**, 88 (2005).

[24] E. Lorch, J. Phys. C: Solid State Phys. **2**, 229 (1969).

[25] V. F. Sears, Neutron News **3**, 26 (1992).

[26] D. Waasmaier and A. Kirfel, Acta Crystallogr., A **51**, 416 (1995).

[27] A. P. Thompson, H. M. Aktulga, R. Berger, D. S. Bolintineanu, W. M. Brown, P. S. Crozier, P. J. in 't Veld, A. Kohlmeyer, S. G. Moore, T. D. Nguyen, R. Shan, M. J. Stevens, J. Tranchida, C. Trott, and S. J. Plimpton, Comput. Phys. Commun. **271**, 108171 (2022).

[28] A. Zeidler, K. Wezka, R. F. Rowlands, D. A. J. Whittaker, P. S. Salmon, A. Polidori, J. W. E. Drewitt, S. Klotz, H. E. Fischer, M. C. Wilding, C. L. Bull, M. G. Tucker, and M. Wilson, Phys. Rev. Lett. **113**, 135501 (2014).

[29] P. S. Salmon, I. Petri, P. H. K. de Jong, P. Verkerk, H. E. Fischer, and W. S. Howells, J. Phys.: Condens. Matter **16**, 195 (2004).

[30] A. Zeidler, P. S. Salmon, H. E. Fischer, J. C. Neuefeind, J. M. Simonson, H. Lemmel, H. Rauch, and T. E. Markland, Phys. Rev. Lett. **107**, 145501 (2011).

[31] M. G. Tucker, D. A. Keen, J. S. O. Evans, and M. T. Dove, J. Phys.: Condens. Matter **19**, 335215 (2007).

[32] A. Zeidler, P. S. Salmon, R. A. Martin, T. Usuki, P. E. Mason, G. J. Cuello, S. Kohara, and H. E. Fischer, Phys. Rev. B **82**, 104208 (2010).

[33] J. Neuefeind and K.-D. Liss, Ber. Bunsenges. Phys. Chem. **100**, 1341 (1996).

[34] M. G. Tucker, D. A. Keen, M. T. Dove, and K. Trachenko, J. Phys.: Condens. Matter **17**, S67 (2005).

[35] C. Sonneville, T. Deschamps, C. Martinet, D. de Ligny, A. Mermet, and B. Champagnon, J. Non-Cryst. Solids **382**, 133 (2013).

[36] L. Huang and J. Kieffer, Phys. Rev. B **69**, 224203 (2004).

[37] L. Huang and J. Kieffer, Phys. Rev. B **69**, 224204 (2004).

[38] L. Stixrude and M. S. T. Bukowinski, Phys. Rev. B **44**, 2523 (1991).

[39] R. J. Hemley, H. K. Mao, P. M. Bell, and B. O. Mysen, Phys. Rev. Lett. **57**, 747 (1986).

[40] F. L. Galeener, Solid State Commun. **44**, 1037 (1982).

[41] A. Pasquarello and R. Car, Phys. Rev. Lett. **80**, 5145 (1998).

[42] A. Rahmani, M. Benoit, and C. Benoit, Phys. Rev. B **68**, 184202 (2003).

[43] M. Guerette, M. R. Ackerson, J. Thomas, F. Yuan, E. B. Watson, D. Walker, and L. Huang, Sci. Rep. **5**, 15343 (2015).

[44] Q. Zhou, Y. Shi, B. Deng, J. Neuefeind, and M. Bauchy, Sci. Adv. **7**, eabh1761 (2021).

[45] C. Meade, R. J. Hemley, and H. K. Mao, Phys. Rev. Lett. **69**, 1387 (1992).

[46] C. J. Benmore, E. Soignard, S. A. Amin, M. Guthrie, S. D. Shastri, P. L. Lee, and J. L. Yarger, Phys. Rev. B **81**, 054105 (2010).

[47] T. Sato and N. Funamori, Phys. Rev. B **82**, 184102 (2010).

[48] Y. Hiraoka, T. Nakamura, A. Hirata, E. G. Escolar, K. Matsue, and Y. Nishiura, Proc. Natl. Acad. Sci. U.S.A. **113**, 7035 (2016).

[49] D. Ormrod Morley, P. S. Salmon, and M. Wilson, J. Chem. Phys. **154**, 124109 (2021).

[50] H. d'Amour, W. Denner, and H. Schulz, Acta Crystallogr., B **35**, 550 (1979).

[51] K. Wezka, P. S. Salmon, A. Zeidler, D. A. J. Whittaker, J. W. E. Drewitt, S. Klotz, H. E. Fischer, and D. Marrocchelli, J. Phys.: Condens. Matter **24**, 502101 (2012).

[52] T. Rouxel, H. Ji, J. P. Guin, F. Augereau, and B. Rufflé, J. Appl. Phys. **107**, 094903 (2010).

[53] T. M. Gross, J. Non-Cryst. Solids **358**, 3445 (2012).

[54] F. Yuan and L. Huang, Sci. Rep. **4**, 5035 (2014).

[55] T. Rouxel, Philos. Trans. R. Soc. A **373**, 20140140 (2015).

[56] P. S. Salmon and L. Huang, MRS Bull. **42**, 734 (2017).

[57] P. S. Salmon, G. S. Moody, Y. Ishii, K. J. Pizzey, A. Polidori, M. Salanne, A. Zeidler, M. Buscemi, H. E. Fischer, C. L. Bull, S. Klotz, R. Weber, C. J. Benmore, and S. G. MacLeod, J. Non-Cryst. Solids: X **3**, 100024 (2019).

[58] S. K. Lee, J. L. Mosenfelder, S. Y. Park, A. C. Lee, and P. D. Asimow, Proc. Natl. Acad. Sci. U.S.A. **117**, 21938 (2020).

[59] P. S. Salmon and A. Zeidler, Data sets for "Ring compaction as a mechanism of densification in amorphous silica," University of Bath Research Data Archive (2023), https://doi.org/10.15125/BATH-01106.